


Optical forces, torques, and force densities calculated at a microscopic level using a self-consistent hydrodynamics method

Kun Ding and C. T. Chan*

Department of Physics and Institute for Advanced Study, The Hong Kong University of Science and Technology, Clear Water Bay, Hong Kong

 (Received 20 July 2017; revised manuscript received 24 March 2018; published 9 April 2018)

The calculation of optical force density distribution inside a material is challenging at the nanoscale, where quantum and nonlocal effects emerge and macroscopic parameters such as permittivity become ill-defined. We demonstrate that the microscopic optical force density of nanoplasmonic systems can be defined and calculated using the microscopic fields generated using a self-consistent hydrodynamics model that includes quantum, nonlocal, and retardation effects. We demonstrate this technique by calculating the microscopic optical force density distributions and the optical binding force induced by external light on nanoplasmonic dimers. This approach works even in the limit when the nanoparticles are close enough to each other so that electron tunneling occurs, a regime in which classical electromagnetic approach fails completely. We discover that an uneven distribution of optical force density can lead to a light-induced spinning torque acting on individual particles. The hydrodynamics method offers us an accurate and efficient approach to study optomechanical behavior for plasmonic systems at the nanoscale.

DOI: [10.1103/PhysRevB.97.155118](https://doi.org/10.1103/PhysRevB.97.155118)

I. INTRODUCTION

Within the framework of classical electrodynamics, optical forces acting on an object can be obtained by integrating electromagnetic stress tensors over a boundary enclosing the object [1,2]. There are different formulations of macroscopic electromagnetic stress tensors [2–6], each of which gives exactly the same result if the boundary is in a vacuum but different results if the boundary cuts across a material [7–14]. If we go one step further to find the distribution of force (force density) within a material, different electromagnetic tensors also yield different results. Which tensor is the correct one is a very complicated issue [8–18]. Calculating the force and force density in nanosystems is even more difficult when quantum effects such as electron “spill-out,” nonlocality, and charge tunneling occur [19–24]. Classical stress tensors that require macroscopic permittivity and permeability simply cannot be used.

An *ab initio* approach that determines microscopic charge/current and fields should be ideal for obtaining optical force densities at the microscopic level for nanosystems. However, most *ab initio* algorithms do not include the retardation effects of external electromagnetic (EM) waves, which can be a problem because optical scattering forces are dominated by retardation. While it is possible to combine *ab initio* density-functional methods with Maxwell equations [25,26], computation is extremely demanding. In this study, we use a self-consistent hydrodynamics model (SC-HDM) [27–30] to calculate microscopic optical force densities in plasmonic systems. This method solves Maxwell equations and the equation of motion for electrons on an equal footing

and can hence provide a description of optical force densities at the microscopic level, taking quantum and retardation effects into account at a reasonable computation cost.

We demonstrate the method by investigating light-induced forces and the microscopic optical force densities of metallic nanoparticle dimers illuminated by an external light source. The microscopic optical force densities also give the optical torque acting on each nanoparticle, and we find a notable spinning torque when the gap size is at the nanometer scale. The optical binding force and spinning torque are closely correlated with the evolution of plasmonic modes as the particles approach each other. The paper is organized as follows. In Sec. II, we briefly review the self-consistent hydrodynamics model, and we show the absorption spectrum of plasmonic dimers. The numerical results of optical force density for plasmonic dimers are given in Sec. III. In Sec. IV, we show absorption spectrum and optical force density for plasmonic bowtie structures. Conclusions are drawn in Sec. V.

II. ABSORPTION SPECTRUM OF DIMERS

We consider two-dimensional configurations in which the particles are cylinders and the k vector of the external EM field is normal to the axis of the cylinders. We use the standard jellium model, which offers an adequate description for simple metals, and SC-HDM is known to be suitable for simple metals [27–30]. We consider sodium particles as our prototype, with ion density n_{ion} defined as $n_{\text{ion}} = \frac{3}{4\pi(r_s a_H)^3}$, where $a_H = 0.529 \text{ \AA}$ is the Bohr radius and the dimensionless quantity $r_s = 4$.

Let us start with the dimer configuration shown in the inset of Fig. 1(b). Two identical plasmonic circular cylinders are placed close to each other, separated by a gap

*Corresponding author: pchan@ust.hk

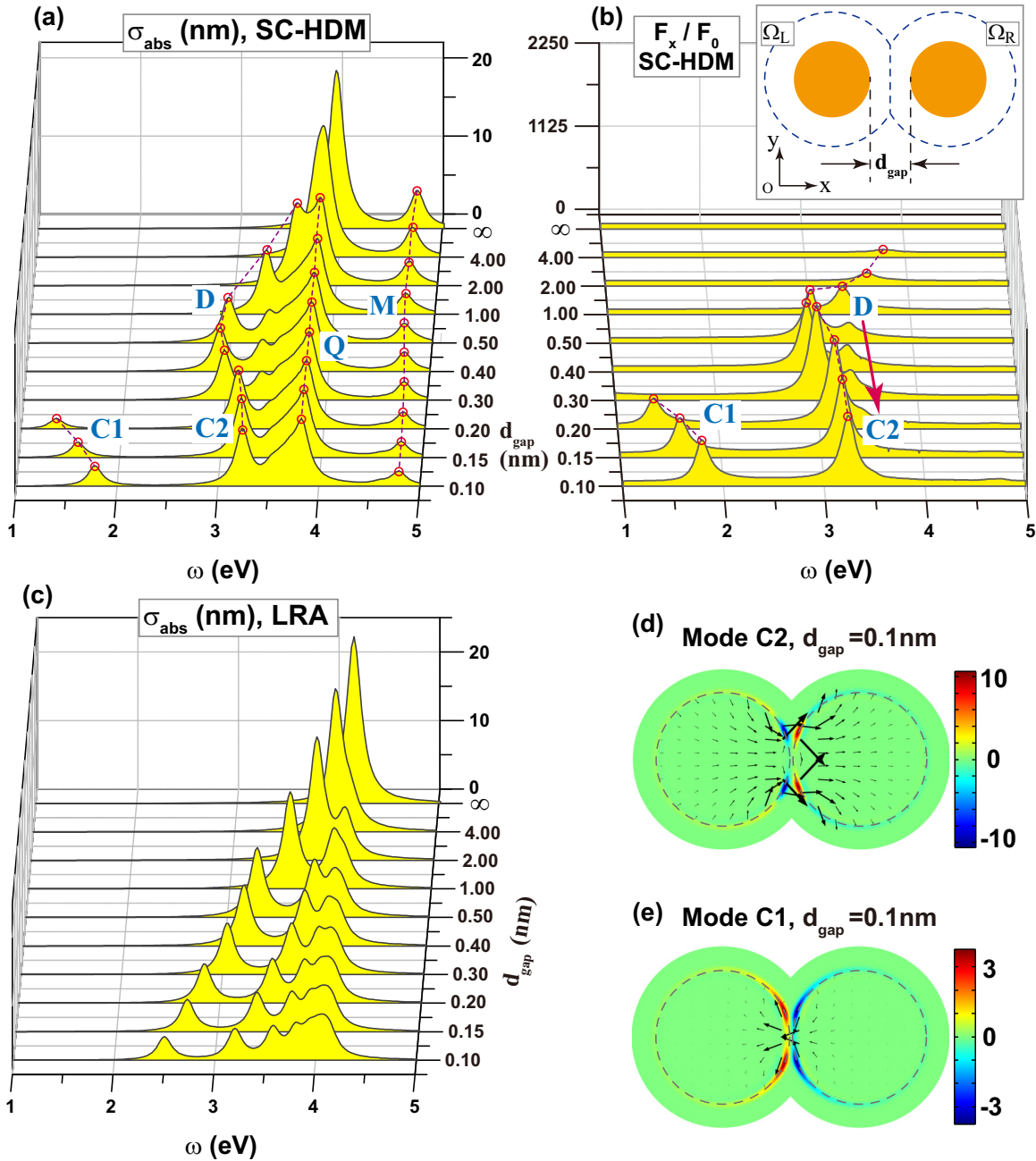


FIG. 1. (a) Absorption cross section σ_{abs} and (b) optical binding force F_x for different separations (d_{gap}) of cylinder dimers under plane-wave illumination with $\mathbf{k}_{\text{inc}} \parallel y$, $\mathbf{E}_{\text{inc}} \parallel x$, and $E_0 = 1.0$ V/m calculated by SC-HDM. For comparison, the absorption spectra calculated by classical local response models are plotted in (c). The radii of both cylinders are 2.0 nm. F_0 is the optical force for a perfect absorber of the same geometric cross section as a single cylinder. The dashed lines and open red circles label different plasmonic modes. The inset in (b) shows a plasmonic cylinder dimer with the yellow region marking the jellium background, and Ω_L and Ω_R are the calculation domains for the left and right particles, respectively. Contour plots of the induced charges ρ_1 / E_0 and arrow plot of the current densities \mathbf{J}_1 at some particular time for (d) C2 mode and (e) C1 mode with $d_{\text{gap}} = 0.1$ nm. The gray dashed lines in (d) and (e) mark the jellium boundaries of these particles.

of size d_{gap} . The yellow regions represent the positively charged jellium background with radii r_a . The first step of SC-HDM involves determining the electronic ground state that minimizes a density functional subjected to constraints (chemical potential and electron number), which requires the numerical calculation of the equilibrium electron density n_0 and effective single-electron potential V_{eff} [31,32]. Once the ground states are obtained, the excited-state calculations can be performed numerically by coupling the linearized

equations of motion for the electron gas with Maxwell equations [31],

$$(-i\omega + \gamma)\mathbf{J}_1 = \frac{en_0}{m_e} \nabla \left(\frac{\delta G}{\delta n} \right)_1 + \frac{e^2 n_0}{m_e} \mathbf{E}_1, \quad (1)$$

$$\nabla \cdot \mathbf{J}_1 - i\omega \rho_1 = 0, \quad (2)$$

$$\nabla \times (\nabla \times \mathbf{E}_1) - \left(\frac{\omega}{c} \right)^2 \mathbf{E}_1 = i\omega \mu_0 \mathbf{J}_1, \quad (3)$$

where $-e$ is the charge of electron ($e > 0$), m_e is the mass of electron, and γ is the loss parameter. The functional $G[n(\mathbf{r}, t)]$ is the internal energy of the electron gas, including terms that describe the internal kinetic energy and the exchange-correlation energy [31]. The inclusion of $G[n(\mathbf{r}, t)]$ is crucial in the SC-HDM because this term gives the quantum tunneling and nonlocal response. Setting $G[n(\mathbf{r}, t)]$ to zero automatically recovers the classical description of metal, namely Drude conductivity [31]. Equations (1)–(3) automatically imply that retardation is included. The induced charge density ρ_1 , current density \mathbf{J}_1 , and microscopic electric (magnetic) fields \mathbf{E}_1 (\mathbf{B}_1) are solved numerically using the ground-state results from the previous step. The incident light propagates in the y direction ($\mathbf{k}_{\text{inc}} \parallel \hat{y}$), and the electric fields are polarized in the x direction, i.e., $\mathbf{E}_{\text{inc}} = \hat{x} E_0 e^{i\mathbf{k}_{\text{inc}} \cdot \mathbf{r}}$ (see Supplemental Material, section I, for numerical details [33]).

The calculated absorption cross sections as a function of frequency for the dimer for different gap sizes calculated by SC-HDM and the classical local response approximation (LRA) are shown in Figs. 1(a) and 1(c), respectively. For comparison, we calculate the absorption spectrum of a single cylinder by setting $d_{\text{gap}} = \infty$, as shown by the panels marked by ∞ in Figs. 1(a) and 1(c). The single-cylinder spectrum calculated by SC-HDM has two peaks. The lower-frequency main peak in Fig. 1(a) is the dipole plasmon resonance, which is redshifted from the classical resonance frequency 4.165 eV [$=\omega_p/\sqrt{2}$, the single peak in Fig. 1(c)]. The redshift is due to the so-called electron spill-out effect [34–36]. The higher-frequency minor peak in Fig. 1(a) is the Bennett plasmon mode (denoted by M), which can only appear in quantum models that can handle electron spill-out effects [37–39]. This mode cannot appear in classical EM calculations, as shown in Fig. 1(c). Figure 1(a) shows that when $d_{\text{gap}} = 4.0 \text{ nm}$, two well-separated absorption peaks remain in the spectrum, which can be traced to those of a single cylinder [29]. Reducing the gap size splits the main absorption peak into two, as is exemplified by the spectrum at $d_{\text{gap}} = 1.0 \text{ nm}$ in Fig. 1(a). The lower-frequency peak is the dipole mode (marked by D), as the induced electric dipoles of the two cylinders are in phase. The higher-frequency peak is a quadrupole mode (denoted by Q). The split between the D and Q modes increases as the gap size decreases. This splitting also appears in the classical model results [40].

When the gap is small enough to allow the tunneling of electrons through it, charge-transfer plasmonic modes (denoted by $C1$ and $C2$) emerge [41,42]. SC-HDM and LRA results are very different in this regime of small gap distances. Let us examine the spectra at the extreme limit of $d_{\text{gap}} = 0.1 \text{ nm}$ shown in Fig. 1(a) at which tunneling can surely occur. We see that in addition to the mode Q and mode M , two plasmonic modes appear, denoted as $C1$ and $C2$, respectively. These charge-transfer plasmonic modes are absent in LRA calculations, as shown in Fig. 1(c). While both $C1$ and $C2$ are charge-transfer modes, they have distinct properties. Examination of the current movement [Fig. 1(e)] suggests that the induced currents flow through the gap in mode $C1$ and the two particles effectively become a long dumbbell. This explains the low frequency of the mode. The mode $C2$ originates from the mode D as can be seen in Fig. 1(a). As shown in Fig. 1(d), we see that the induced charge distributions of the D mode (see

Supplemental Material, section II, for details) and $C2$ mode are similar except near the gap region, which means the $C2$ mode can be treated as a charge-transfer-corrected D mode. These charge-transfer modes are consistent with *ab initio* [41–47] and experimental results [48–53] observed in similar systems, indicating that our SC-HDM calculations capture the essential physics of such systems (see Supplemental Material, section II, for details [33]).

III. OPTICAL FORCE DENSITY

We now come to the force calculations. As the magnitude of optical forces depends strongly on resonances, the results shown in Fig. 1 show that optical forces cannot be calculated reliably using LRA, which fails to describe the resonance correctly. There is another level of subtlety. Optical forces are usually calculated using various forms of electromagnetic stress tensors, as specified by the macroscopic local permittivity ϵ and permeability μ of the material. In the nanoscale, when nonlocality and quantum effects become important, local macroscopic constitutive parameters become meaningless. We need to employ the microscopic fields. Our method becomes handy as it can determine the microscopic electric and magnetic fields, allowing us to calculate the light-induced optical force and torque without using macroscopic values of ϵ and μ . Microscopic induced charges and currents are available point by point and can be used to calculate the force density. Within the SC-HDM framework, the time-averaged optical forces due to a time-harmonic external field can be calculated by examining the time-averaged Lorentz force densities of the electron gas, defined as $\mathbf{f} = \langle \rho_1 \mathbf{E}_1 + \mathbf{J}_1 \times \mathbf{B}_1 \rangle$, in which \mathbf{E}_1 and \mathbf{B}_1 are microscopic fields including both incident and scattering fields. The force density distributions and the integrated total forces are shown in Fig. 2. Same as the configuration shown in the inset of Fig. 1, the incident light propagates in the y direction with electric field polarized along the x direction. Integrating the y component of the time-averaged Lorentz force densities in the entire calculation domain ($\mathbf{F}_y = \int_{\Omega_T} \mathbf{f}_y \, d\mathbf{r}$) gives the total optical forces acting on the system in the direction of the incident light, as shown by the solid blue lines in Fig. 2(a) for $d_{\text{gap}} = 0.1 \text{ nm}$. Each peak in the total optical force spectrum can be identified with a corresponding absorption peak and labeled accordingly, as shown in Fig. 1(a). The absorption and the optical force spectra are correlated because the particle gains mechanical momentum after absorbing incident photons. For comparison, we also calculate the total optical forces by finding the surface integral of the time-averaged Maxwell stress tensor $\langle \mathbf{T} \rangle$ in the far field, as shown by the red open circles in Fig. 2(a). The results calculated using the Lorentz force formula and the Maxwell tensor are the same because we are using microscopic fields.

We plot the force distribution of \mathbf{f}_y for the charge-transfer modes $C1$ and $C2$ in Figs. 2(b) and 2(c), respectively, when $d_{\text{gap}} = 0.1 \text{ nm}$. We observe that the optical force density is concentrated in a very small region along the boundary, and the y component of the optical force density for the dimer is at a maximum near the vacuum gaps but not at the smallest gap position when tunneling occurs. The sign of the force density changes near the gap (red/blue color in Fig. 2), indicating that the surfaces near the gap experience large stresses. The

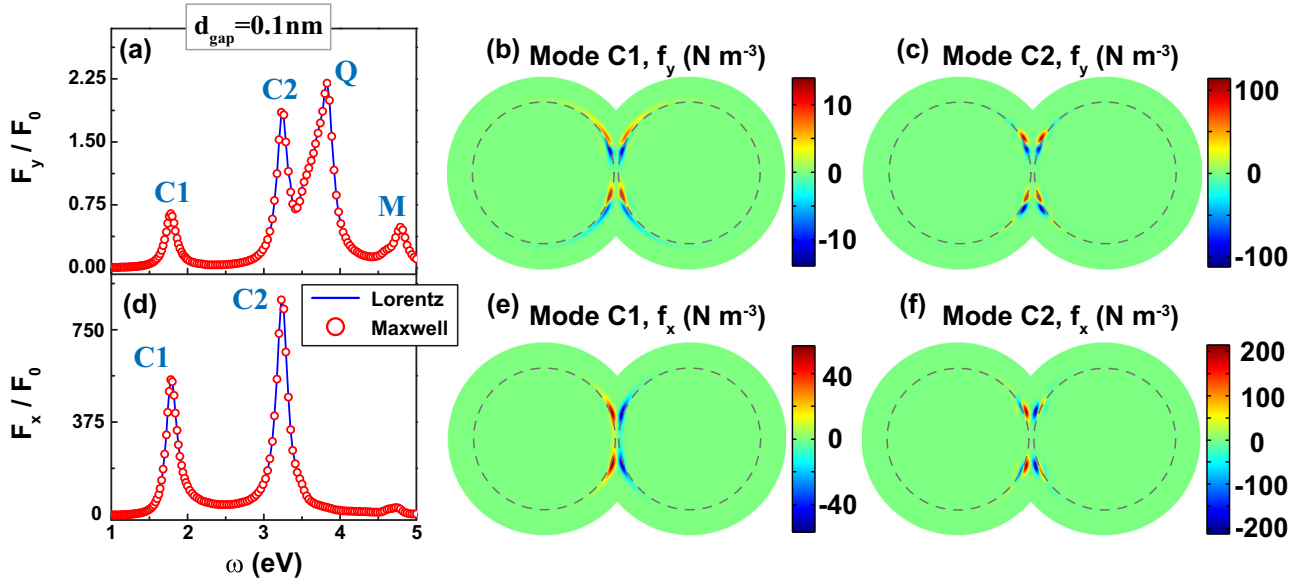


FIG. 2. (a) Total force in the y direction and (d) optical binding forces (x direction) for $d_{\text{gap}} = 0.1$ nm. Note the agreement between results obtained by integrating Lorentz force density (solid blue lines) and Maxwell stress tensor (red open circles). (b) and (c) show the y components of Lorentz force densities for modes C1 and C2, respectively. (e) and (f) show the x components. The gray dashed lines in (b), (c), (e), (f) mark the jellium boundaries of these particles.

magnitude of the optical force density for the C2 mode is one order larger than that of the C1 mode, consistent with the total force results in Fig. 2(a).

The distribution of \mathbf{f}_x for these charge-transfer modes is shown in Figs. 2(e) and 2(f), respectively. Similarly to the y component, the x component of the force density is concentrated in a small boundary region but is one order of magnitude larger than \mathbf{f}_y , although the incident light momentum is in the y direction. These perpendicular optical force densities play the central role in the optical binding forces, which are used in optical manipulations [54–58]. If the particles are well separated, the optical binding forces can be obtained using classical electrodynamics, but more sophisticated methods must be used when the particles are so close that nonlocality is important or when tunneling occurs. Here, we can obtain the optical binding forces by calculating the volume integral of the time-averaged Lorentz force density in the left (or right) particle calculation domain Ω_L (Ω_R) as $\mathbf{F}_x = \int_{\Omega_L} \mathbf{f}_x \, d\mathbf{r}$. The domain Ω_L and Ω_R is chosen to be symmetric about the y axis, and the boundaries of these domains are shown by the dashed lines in Fig. 1(b). The calculated optical binding force spectra as a function of various gap sizes are shown in Fig. 1(b). As the magnitude of light-induced forces depends on external light intensity, we normalize the calculated force with respect to F_0 , which is the optical force of a perfect absorber of the same geometric cross section as a single cylinder. We find a significant attractive force acting on each particle and hence a light-induced binding force between these two particles. For comparison, we also calculate the surface integral of time-averaged Maxwell stress tensor $\langle \mathbf{T} \rangle \cdot \hat{\mathbf{n}} \, d\mathbf{S}$ on the boundary of the domain Ω_L , namely $\int_{\partial\Omega_L} \langle \mathbf{T} \rangle \cdot \hat{\mathbf{n}} \, d\mathbf{S}$. The results are plotted by the red open circles in Fig. 2(d) for $d_{\text{gap}} = 0.1$ nm. Comparing Figs. 2(a) and 2(d), we see that the forward-scattering force (y direction) can be slightly enhanced by resonance, which can

also be seen from the absorption cross section in Fig. 1(a), but the optical binding forces (x direction) are significantly amplified (by hundreds of times the value of F_0) although it is in the transverse direction. These excellent agreements demonstrate that if the microscopic charges, currents, and fields can be obtained, then a Maxwell stress tensor is the only suitable choice for calculating the surface integral.

Some remarks are in order here. The results shown in Figs. 2(a) and 2(d) suggest that a Maxwell stress tensor together with the microscopic fields gives exactly the same result of the microscopic force densities as those computed using Lorentz force formula (as it must be). This confirms the fact the ambiguity on what is the correct electromagnetic stress tensor to use (e.g., Abraham vs Einstein-Laub [4,6]) arises because macroscopic parameters are used. If microscopic field quantities are used, there is no ambiguity, and our method provides a recipe to do force calculations without using macroscopic parameters such as ϵ and μ . In addition, the microscopic force densities give us all the details of the optical forces, and hence we could predict the optomechanical behavior of our system, such as spinning torque, which we will discuss later.

Comparing Fig. 1(a) with Fig. 1(b), we find that not all absorption resonance gives rise to optical binding. Strong binding forces are found for the mode D (which becomes C2 when tunneling occurs). We plot the magnitudes of these maximum binding forces for various values of d_{gap} in Fig. 3(a). The binding force increases rapidly as the gap size decreases, reaching a maximum at $d_{\text{gap}} \cong 0.3$ nm. When the gap size further decreases, the binding force drops due to the charge transfer in the gap. If we naively assume that the electromagnetic energy stored in the dimer is dominated by one mode, the energy can be written as $U = N\hbar\omega$, where N is the number of photons in the resonance mode. The binding forces can then be written as $F = -\frac{\partial U}{\partial x} = -N\hbar \frac{\partial \omega}{\partial x}$. Consider

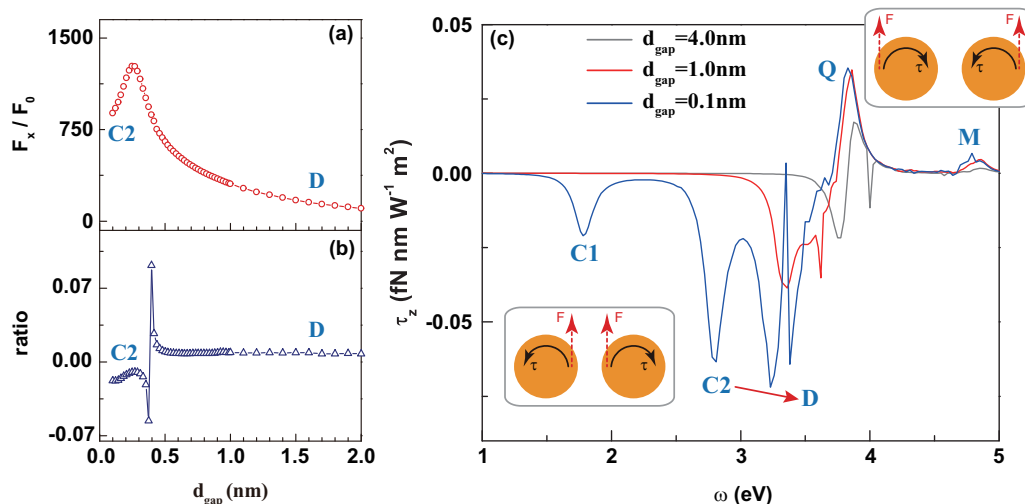


FIG. 3. (a) Maximum optical binding forces as a function of gap sizes. (b) The ratio, defined as $F_x / (\partial \omega_{D,C2} / \partial d_{\text{gap}})$, as a function of gap size. (c) Optical torque (z component, normalized to per unit length) acting on the cylinder on the right for $d_{\text{gap}} = 4.0, 1.0$, and 0.1 nm. The insets show that the location of maximum force densities (red dotted arrow) determines the sense of rotation (black arrow).

the ratio as $F_x / (\frac{\partial \omega_{D,C2}}{\partial d_{\text{gap}}})$, which is plotted in Fig. 3(b). A constant ratio indicates that the character of this mode remains the same; otherwise the mode must change to other modes. When $d_{\text{gap}} > 0.5$ nm, the ratio is nearly constant. A sharp transition occurs at $d_{\text{gap}} < 0.5$ nm, which can be used as a marker to characterize the transition between the dipole (D mode) and charge-transfer mode ($C2$). The binding forces of the $C1$ mode are also substantial for small gap sizes. These results suggest that the optical binding forces offer a useful indicator of changes in plasmonic modes as system configuration changes that may otherwise be much more tedious to trace (such as by examining mode profiles).

The microscopic optical force densities can also be used to qualitatively predict the behavior of the system. For example, visual examination of Figs. 2(b) and 2(c) indicates that there must be a light-induced spinning torque acting on each cylinder as the force densities in each cylinder are not symmetric about their own center. We calculate the optical torque of the right cylinder by calculating the volume integral $\tau = \int_{\Omega_R} (\mathbf{r} - \mathbf{r}_c) \times \mathbf{f} \, d\mathbf{r}$, where \mathbf{r}_c is the center of the right cylinder. Figure 3(c) shows the z component of the optical torque for $d_{\text{gap}} = 4.0$ nm, $d_{\text{gap}} = 1.0$ nm, and $d_{\text{gap}} = 0.1$ nm, respectively. We observe that the torque is negative (rotating clockwise for the right cylinder) for the charge-transfer plasmonic modes and the D mode and positive for the Q mode. This is because in the $C1$, $C2$, and D modes, the optical force densities are higher near the gap regions, and the force direction is in the general direction of light propagation (red arrows), and so the right/left cylinder rotates in the clockwise/counterclockwise direction, as shown in the left inset of Fig. 3(c). On the contrary, the optical force densities for the Q mode are lower near the gap regions, and hence the right/left cylinder rotates in the counterclockwise/clockwise directions. For comparison, we also calculate these spinning torques using Drude models (see Supplemental Material, section III [33]). At the nanoscale, absorption spectra of classical model and SC-HDM are different, but the spinning torques are still nonzero, which highlights these torques are significant at the nanoscale.

We note that optical forces and torques acting on plasmonic particles have attracted attention recently and have been experimentally studied (see for example Refs. [59–62]). In these experiments, the systems are in mechanical equilibrium in the absence of light, and the optical forces/torques act as a perturbation, indicating that the system is still in a quasiequilibrium state. Numerical calculation can be carried out assuming that the electrons move much faster than any type of displacement or spinning movement of the particle, so that even if the particles are moving or starting to move, the electronic density can be determined at the instantaneous position of the particle. Another approximation is that we ignore the possible deformation caused by optical forces. This is an excellent approximation because internal elastic forces are much larger than optical force density shown in Fig. 2. For example, internal force densities due to chemical bonding are at least on the order of 10^{19} N m⁻³, which is several orders of magnitude bigger than optical force density. We also note that the optical binding force and spinning torque presented previously are experimentally measurable quantities, particularly in a liquid environment [60].

IV. OPTICAL FORCE DENSITY OF BOWTIE STRUCTURES

To demonstrate the versatility of the method, we perform similar calculations for two sodium triangles (Fig. 4). The calculated absorption spectra for different gap sizes are shown in Fig. 4(a). When the gap size is large, the absorption spectrum is similar to that of a single triangle, with three major absorption peaks in the spectrum (two edge modes and one face mode [31]). With a decreasing d_{gap} , the fundamental edge mode (Ed_1) transitions to the charge-transfer mode $C2$, and another charge-transfer mode $C1$ appears. We show the x component of optical force density for the modes $C1$ and $C2$ in Figs. 4(e) and 4(f), respectively. The maximum force density also occurs near the vacuum gap, similarly to the cylinder dimer. The maximum binding force occurs in the modes Ed_1 and $C2$. To illustrate the mode transitions, we also

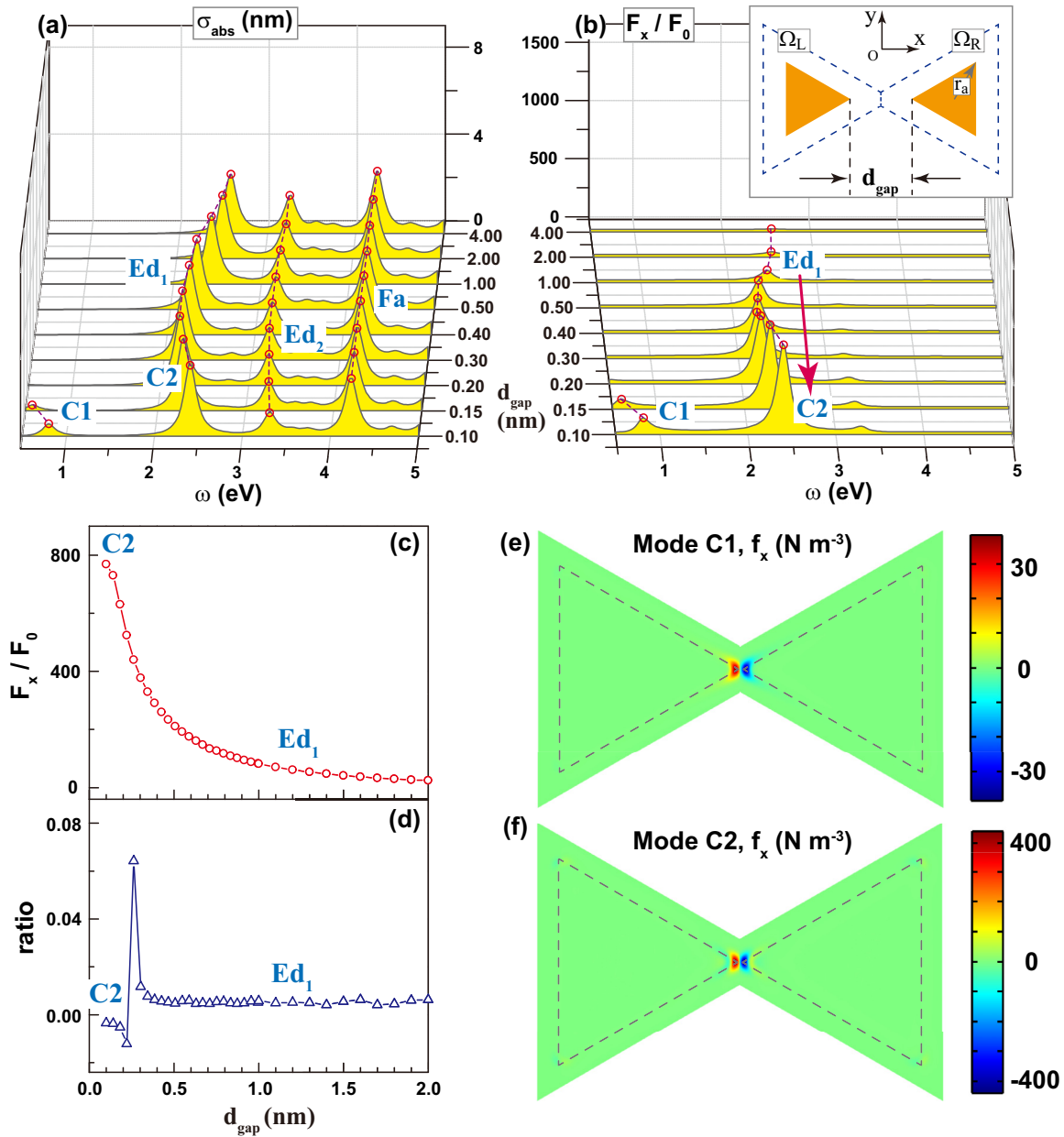


FIG. 4. (a) Absorption cross section σ_{abs} and (b) optical binding force for decreasing gap sizes of the two-triangle dimer (illustrated in the inset) under single plane-wave illumination with $\mathbf{k}_{\text{inc}} \parallel y$, $\mathbf{E}_{\text{inc}} \parallel x$ and $E_0 = 1.0$ V/m. The circumradius of both triangles is 2.0 nm. The dashed lines and open circles mark different plasmonic modes. (c) The maximum optical binding force as a function of gap size. (d) The ratio, defined as $\mathbf{F}_x / (\partial \omega_{Ed1, C2} / \partial d_{\text{gap}})$, as a function of gap size. The x component of Lorentz force density for the modes C1 and C2 are plotted in (e) and (f), respectively. The gray dashed lines in (e) and (f) mark the jellium boundaries of these particles.

plot the optical binding forces between these two triangles for different gap sizes in Fig. 4(b) and plot the maximum binding force as a function of d_{gap} in Fig. 4(c). The ratio $\mathbf{F}_x / (\frac{\partial \omega_{Ed1, C2}}{\partial d_{\text{gap}}})$ is plotted in Fig. 4(d), which shows that the mode transition from Ed_1 to C2 occurs at $d_{\text{gap}} \cong 0.4$ nm. The binding forces in the C2 mode are also greater than in the C1 mode. As a result, the binding forces can still quantitatively predict the mode transitions in the bowtie structures, similarly to the two-cylinder dimer configuration. In addition, the spinning torque for each triangle induced by external light is also nonzero but one order of magnitude smaller than that of the cylinder (see Supplemental Material, section III [33]).

We note that the Lorentz force is the electromagnetic force term that depends linearly on external fields. There are other internal force terms, such as those of the electron fluid due to changes in the local chemical potential. In addition, there are chemical bonding forces which in the language of density-functional theory (DFT) are called Hellmann-Feynman forces that are determined by the electronic eigenstates, which are weakly dependent on the external field. These quantum forces do not depend explicitly on external fields and are not included in our electromagnetic force consideration. They should be calculated using DFT if desired. All of these forces have a short range and exist even in the absence of external EM waves,

but the optical binding forces here are caused explicitly by the scattering of EM waves between these two particles and are therefore fairly long-range forces, as shown in Fig. 3(a).

V. CONCLUSION

In summary, we have calculated the microscopic optical force densities for dimerized nanoplasmonic particles using a self-consistent hydrodynamic model. We show that the microscopic optical force density and binding forces can be defined and calculated although quantum effects and nonlocality are

significant. Furthermore, the binding force spectrum provides a useful method of tracing plasmonic mode evolution. We also show that the uneven distribution of optical force density can lead to a strong spinning torque acting on each nanoparticle.

ACKNOWLEDGMENTS

We thank Prof. Z. Q. Zhang, Prof. Zhifang Lin, and Prof. Jack Ng for helpful discussions. This work is supported by Research Grants Council, University Grants Committee, Hong Kong (Grant No. AOE/P-02/12).

-
- [1] J. D. Jackson, *Classical Electrodynamics* (John Wiley & Sons, Hoboken, NJ, 1999).
- [2] L. D. Landau, E. M. Lifshitz, and L. P. Pitaevskii, *Electrodynamics of Continuous Media* (Butterworth-Heinemann, Oxford, 1995).
- [3] I. Brevik, *Phys. Rep.* **52**, 133 (1979).
- [4] M. Abraham, *Rend. Circ. Mat. Palermo* **30**, 33 (1910).
- [5] H. Minkowski, *Math. Ann.* **68**, 472 (1910).
- [6] A. Einstein and J. Laub, *Ann. Phys.* **331**, 541 (1908).
- [7] S. M. Barnett, *Phys. Rev. Lett.* **104**, 070401 (2010).
- [8] W. J. Sun, S. B. Wang, J. Ng, L. Zhou, and C. T. Chan, *Phys. Rev. B* **91**, 235439 (2015).
- [9] I. Liberal, I. Ederra, R. Gonzalo, and R. W. Ziolkowski, *Phys. Rev. A* **88**, 053808 (2013).
- [10] M. Mansuripur, A. R. Zakharian, and E. M. Wright, *Phys. Rev. A* **88**, 023826 (2013).
- [11] A. M. Jazayeri and K. Mehrany, *Phys. Rev. A* **89**, 043845 (2014).
- [12] V. Kajorndejnukul, W. Ding, S. Sukhov, C.-W. Qiu, and A. Dogariu, *Nat. Photon.* **7**, 787 (2013).
- [13] C.-W. Qiu, W. Ding, M. R. C. Mahdy, D. Gao, T. Zhang, F. C. Cheong, A. Dogariu, Z. Wang, and C. T. Lim, *Light Sci. Appl.* **4**, e278 (2015).
- [14] M. Sonnleitner, M. Ritsch-Marte, and H. Ritsch, *New J. Phys.* **14**, 103011 (2012).
- [15] B. A. Kemp, J. A. Kong, and T. M. Grzegorzczak, *Phys. Rev. A* **75**, 053810 (2007).
- [16] V. Yannopoulos and P. G. Galiatsatos, *Phys. Rev. A* **77**, 043819 (2008).
- [17] V. G. Veselago, *Phys. Usp.* **52**, 649 (2009).
- [18] S. Wang, J. Ng, M. Xiao, and C. T. Chan, *Sci. Adv.* **2**, e1501485 (2016).
- [19] Y. Luo, R. Zhao, and J. B. Pendry, *Proc. Natl. Acad. Sci. USA* **111**, 18422 (2014).
- [20] C. Ciraci, R. T. Hill, J. J. Mock, Y. Urzhumov, A. I. Fernández-Domínguez, S. A. Maier, J. B. Pendry, A. Chilkoti, and D. R. Smith, *Science* **337**, 1072 (2012).
- [21] J. A. Scholl, A. L. Koh, and J. A. Dionne, *Nature (London)* **483**, 421 (2012).
- [22] W. Yan, M. Wubs, and N. Asger Mortensen, *Phys. Rev. Lett.* **115**, 137403 (2015).
- [23] C. P. Byers, H. Zhang, D. F. Swearer, M. Yorulmaz, B. S. Hoener, D. Huang, A. Hoggard, W.-S. Chang, P. Mulvaney, E. Ringe, N. J. Halas, P. Nordlander, S. Link, and C. F. Landes, *Sci. Adv.* **1**, e1500988 (2015).
- [24] D. Jin, Q. Hu, D. Neuhauser, F. von Cube, Y. Yang, R. Sachan, T. S. Luk, D. C. Bell, and N. X. Fang, *Phys. Rev. Lett.* **115**, 193901 (2015).
- [25] K. Yabana, T. Sugiyama, Y. Shinohara, T. Otobe, and G. F. Bertsch, *Phys. Rev. B* **85**, 045134 (2012).
- [26] S. A. Sato, K. Yabana, Y. Shinohara, T. Otobe, and G. F. Bertsch, *Phys. Rev. B* **89**, 064304 (2014).
- [27] E. Zaremba and H. C. Tso, *Phys. Rev. B* **49**, 8147 (1994).
- [28] W. Yan, *Phys. Rev. B* **91**, 115416 (2015).
- [29] G. Toscano, J. Straubel, A. Kwiatkowski, C. Rockstuhl, F. Evers, H. Xu, N. A. Mortensen, and M. Wubs, *Nat. Commun.* **6**, 7132 (2015).
- [30] C. Ciraci and F. Della Sala, *Phys. Rev. B* **93**, 205405 (2016).
- [31] K. Ding and C. T. Chan, *Phys. Rev. B* **96**, 125134 (2017).
- [32] COMSOL Multi-physics 4.4, developed by COMSOL Inc. (2013).
- [33] See Supplemental Material at <http://link.aps.org/supplemental/10.1103/PhysRevB.97.155118> for details about our model.
- [34] P. J. Feibelman, *Phys. Rev. B* **40**, 2752 (1989).
- [35] A. Liebsch, *Phys. Rev. B* **48**, 11317 (1993).
- [36] W. L. Schaich, *Phys. Rev. B* **55**, 9379 (1997).
- [37] A. J. Bennett, *Phys. Rev. B* **1**, 203 (1970).
- [38] K.-D. Tsuei, E. W. Plummer, A. Liebsch, K. Kempa, and P. Bakshi, *Phys. Rev. Lett.* **64**, 44 (1990).
- [39] G. Chiarello, V. Formoso, A. Santaniello, E. Colavita, and L. Papagno, *Phys. Rev. B* **62**, 12676 (2000).
- [40] J. B. Pendry, A. Aubry, D. R. Smith, and S. A. Maier, *Science* **337**, 549 (2012).
- [41] T. V. Teperik, P. Nordlander, J. Aizpurua, and A. G. Borisov, *Phys. Rev. Lett.* **110**, 263901 (2013).
- [42] L. Stella, P. Zhang, F. J. García-Vidal, A. Rubio, and P. García-González, *J. Phys. Chem. C* **117**, 8941 (2013).
- [43] T. V. Teperik, P. Nordlander, J. Aizpurua, and A. G. Borisov, *Opt. Express* **21**, 27306 (2013).
- [44] D. C. Marinica, A. K. Kazansky, P. Nordlander, J. Aizpurua, and A. G. Borisov, *Nano Lett.* **12**, 1333 (2012).
- [45] D. K. Gramotnev, A. Pors, M. Willatzen, and S. I. Bozhevolnyi, *Phys. Rev. B* **85**, 045434 (2012).
- [46] S.-W. Chang, C.-Y. A. Ni, and S. L. Chuang, *Opt. Express* **16**, 10580 (2008).
- [47] L. Lin and Y. Zheng, *Sci. Rep.* **5**, 14788 (2015).
- [48] F. Wen, Y. Zhang, S. Gottheim, N. S. King, Y. Zhang, P. Nordlander, and N. J. Halas, *ACS Nano* **9**, 6428 (2015).

- [49] A. Ahmadvand, R. Sinha, B. Gerislioglu, M. Karabiyik, N. Pala, and M. Shur, *Opt. Lett.* **41**, 5333 (2016).
- [50] S. Dodson, M. Haggui, R. Bachelot, J. Plain, S. Li, and Q. Xiong, *J. Phys. Chem. Lett.* **4**, 496 (2013).
- [51] N. Yu, E. Cubukcu, L. Diehl, D. Bour, S. Corzine, J. Zhu, G. Höfler, K. B. Crozier, and F. Capasso, *Opt. Express* **15**, 13272 (2007).
- [52] W. Ding, R. Bachelot, S. Kostcheev, P. Royer, and R. E. de Lamaestre, *J. Appl. Phys.* **108**, 124314 (2010).
- [53] M. Kaniber, K. Schraml, A. Regler, J. Bartl, G. Glashagen, F. Flassig, J. Wierzbowski, and J. J. Finley, *Sci. Rep.* **6**, 23203 (2016).
- [54] K. Dholakia and P. Zemánek, *Rev. Mod. Phys.* **82**, 1767 (2010).
- [55] F. Dapasse and J.-M. Vigoureux, *J. Phys. D* **27**, 914 (1994).
- [56] T. M. Grzegorzcyk, B. A. Kemp, and J. A. Kong, *Phys. Rev. Lett.* **96**, 113903 (2006).
- [57] X. Yang, Y. Liu, R. F. Oulton, X. Yin, and X. Zhang, *Nano Lett.* **11**, 321 (2011).
- [58] M.-T. Wei, J. Ng, C. T. Chan, and H. D. Ou-Yang, *Sci. Rep.* **6**, 38883 (2016).
- [59] D. Guan, Z. H. Hang, Z. Marcet, H. Liu, I. I. Kravchenko, C. T. Chan, H. B. Chan, and P. Tong, *Sci. Rep.* **5**, 16216 (2015).
- [60] M. Liu, T. Zentgraf, Y. Liu, G. Bartal, and X. Zhang, *Nat. Nanotechnol.* **5**, 570 (2010).
- [61] V. Shvedov, A. R. Davoyan, C. Hnatovsky, N. Engheta, and W. Krolikowski, *Nat. Photon.* **8**, 846 (2014).
- [62] D. B. Ruffner and D. G. Grier, *Phys. Rev. Lett.* **109**, 163903 (2012).